International Journal of Heat and Mass Transfer 261 (2026) 128596

Contents lists available at ScienceDirect

International Journal of Heat and Mass Transfer

journal homepage: www.elsevier.com/locate/ijhmt

Tailored flow condensation of low surface tension fluids via additively manufactured gradient wick structures

Durga Prasad Ghosh [a], Vivek Mano Mohan [a], Mohammad Reza Shaeri [b], Sajjad Bigham [a,*]

[a] Department of Mechanical and Aerospace Engineering, North Carolina State University, Raleigh, NC, 27695-7910, USA
[b] Advanced Cooling Technologies, Inc., Lancaster, PA, 17601, USA

ARTICLE INFO

Keywords:
Gradient wick flow condenser
3D-printed flow condenser
Tailored flow condensation
Pore size distribution
Low surface tension fluid

ABSTRACT

State-of-the-art enhanced flow condensation techniques perform poorly with low surface tension fluids due to unfavorable filmwise condensation behavior and limited long-term durability. To overcome this challenge, a novel internal flow condenser is developed to tailor flow condensation of commonly used low surface tension fluids by accounting for spatial variations in two-phase flow characteristics. The proposed design conceptualizes gradient wick structures with tuned pore size distributions that reflect the local vapor quality and convective effects as vapor gradually transitions to liquid, while enabling capillary-assisted condensate drainage. Experiments were employed to establish the effectiveness of the gradient wick flow condenser concept against a benchmark uniform wick flow condenser of a similar average porosity. The gradient wick flow condenser, featuring progressively narrowing pores in both longitudinal and lateral directions, not only outperformed the uniform wick flow condenser but also demonstrated a tailored flow condensation performance. In particular, the gradient wick flow condenser unveiled an increase in the local condensation heat transfer coefficient as vapor quality decreases, which is in sharp contrast to conventional flow condensers that suffer declining condensation rates due to condensate film thickening. Additionally, a semi-analytical model was developed to elucidate local flow condensation physics associated with the gradient and uniform wick flow condensers. Findings of the present study underscore the promise of gradient wick flow condensers in enhancing flow condensation performance of extremely wetting fluids such as dielectrics and refrigerants in future thermal management systems.

1. Introduction

Flow condensation is a ubiquitous phenomenon and can be found at the heart of many industrial processes, including data center and chip cooling, refrigeration and air conditioning systems, atmospheric water harvesting, thermal desalination systems, and power generation cycles, among others. Enhancing the two-phase performance of flow condensers is a promising approach to significantly lower energy consumption, reduce size and weight, and minimize the environmental impacts of the above industrial processes. Most previous studies on condensation have focused on enhancing external condensation by promoting the dropwise mode, examining a wide range of strategies, including but not limited to hydrophobic and omniphobic surfaces [1,2], hybrid hydrophobic-hydrophilic surfaces [3], jumping droplet [4,5], gradient capillary structures for decoupling droplet nucleation/growth dynamics from condensate shedding [6–11], and lubricant-infused surfaces [12–14], among others. However, when adapted to internal flow condensation, the dropwise mode exhibits only a 20–66 % improvement [15–17], in contrast to nearly one order-of-magnitude enhancement [18,19] observed in external condensation. Moreover, the effectiveness of the dropwise condensation mode diminishes in the case of low surface tension fluids. As such, the filmwise mode is dominant in many flow condensers employing extremely wetting fluids such as fluorinated dielectrics and refrigerants. Therefore, the development of enhanced filmwise strategies for future flow condensers is of paramount importance.

In recent years, there have been several notable strategies to augment the internal flow condensation process by employing various techniques, including hydrophobic micro-nanostructured/coated channels [16,20], hydrophilic micro-nanostructured/coated channels [15,21], hybrid hydrophobic-hydrophilic channels [22], jumping droplets in internal flow [23], and finned structured channels [24,25]. Cheng et al. [16] performed internal dropwise condensation experiments utilizing water in a hydrophobic tube. Their investigation revealed that

* Corresponding author.
E-mail address: sbigham@ncsu.edu (S. Bigham).

https://doi.org/10.1016/j.ijheatmasstransfer.2026.128596
Received 6 November 2025; Received in revised form 16 February 2026; Accepted 22 February 2026
Available online 26 February 2026

compared to non-coated tubes, the hydrophobic dropwise condensation can enhance internal condensation heat transfer coefficients by 50 %. In contrast to a hydrophobic coating approach, Mendizábal et al. [15] examined superhydrophilic micro-nanostructured copper and aluminum tubes to enhance internal condensation of R1233zd(E) refrigerant. Their results indicated that while microstructured aluminum tubes demonstrated a 66 % increase in the heat transfer coefficient for complete phase change from saturated vapor to saturated liquid, nanostructured copper tubes did not show the same effectiveness in improving the heat transfer coefficient. Bashar et al. [24] examined the condensation heat transfer of R1234yf in smooth and micro-fin tubes. Their results show that while the micro-fin tube establishes a noticeably higher heat transfer coefficient than the smooth tube at partial condensation (e.g., 7.5 vs. 2.5 kW/m^2-K at a vapor quality of 0.5 and a mass velocity of 100 kg/m^2-s), the enhancement substantially diminishes at near full condensation. However, although micro- and nanostructured or coated channels have shown improved internal flow condensation performance, they oftentimes suffer from durability issues under liquid shear and thermal cycling, leading to rapid performance degradation. In addition, conventional fabrication methods such as machining, etching, or coating restrict the ability to create robust, 3D, or spatially varying features, while also increasing complexity and cost, limiting their broader applicability.

Equally important as the previous discussion, prior research on internal flow condensation of low surface tension fluids has indicated a gradual decline in the flow condensation performance as vapor quality decreases during the vapor-to-liquid transition. Kim and Mudawar [26] conducted experiments with the FC-72 dielectric fluid in a square copper microchannel with a hydraulic diameter of 1 mm. They observed that the heat transfer coefficient is highest near the inlet, where the film thickness is the least, and gradually decreases along the condenser length as the film thickness increases. Mattiuzzo et al. [27], conducting flow condensation experiments with R1233zd(E) in small channels, reported similar results. They reported that, at a saturation temperature of 40 °C and a mass flux of 400 kg/m^2-s in a tube with an internal diameter of 0.96 mm, the condensation heat transfer coefficient decreases from ~9.3 to ~3 kW/m^2-K when the vapor quality decreases from ~0.63 to ~0.05, respectively. One strategy explored to counteract the adverse effects of condensate film thickening on the flow condensation performance is the localized drainage of the condensate. Lin and Wang [28] examined this concept by incorporating a micro drainage system aimed at reducing film thickness. They conducted condensation experiments with the HFE-7100 dielectric fluid in microchannel heat sinks with a hydraulic diameter of 800 μm. Their results showed that the micro-drainage channels offer 5–15 % enhancement in the condensation heat transfer coefficient. However, the localized drainage of the condensate introduces additional complexities to the flow condensation process with an increased risk of vapor bypass through the drainage channels. As such, the development of passive strategies, including heat transfer features considering variations in the two-phase flow characteristics, to alleviate the adverse influence of condensate film thickening on flow condensation performance, is of high interest.

More recently, there has been an increased interest in leveraging additive manufacturing (AM) for the realization of advanced flow condenser technologies, as it offers design freedom for fabricating intricate and durable heat transfer geometries suitable for long-term operations. Ho et al. [29] utilized selective laser melting (SLM) to fabricate a 3D cylindrical pin fin condenser, achieving a ~60 % increase in average heat transfer coefficient (HTC) at a fin height of 1.28 mm, a fin diameter of 0.3 mm, and a fin height-to-diameter ratio of 4.27 compared to a smooth surface. In a subsequent study [30], they investigated condensation on sinusoidal pin fin arrays, where nine surfaces with an identical base diameter of 1.24 mm but varying heights and pitches were 3D printed via SLM. Results showed that increasing the fin height-to-diameter ratio from 1 to 1.34 at fixed pitches of 1.25 and 1.67 mm enhanced condensation performance for both geometries, while a further increase in the fin height-to-diameter ratio to 2 reduced the condensation heat flux and HTC. Compared to a smooth surface, a maximum thermal enhancement factor of 1.86 was achieved at a fin height-to-diameter ratio of 1.34 and a fin height-to-pitch ratio of 1. Zaki et al. [31] reported the design, fabrication, and testing of a 3D-printed water-cooled R134a condenser heat exchanger incorporating internal three-dimensional geometries unattainable by conventional methods. A physics-based model coupled with CFD simulations guided the optimization of alternating water and refrigerant channels featuring wavy fins on the water side and chevrons on the refrigerant side. Experimental results showed heat transfer rates of 3–8 kW at refrigerant saturation temperatures of 35–49 °C, with a maximum volumetric power density of 6.2 MW/m^3. Compared to conventional shell-and-tube condensers, the AM design achieved 30–50 % higher performance at similar normalized pumping power, demonstrating a robust framework for developing compact, high-efficiency AM heat exchangers. Ahmadi et al. [32] developed and evaluated a novel 3D-printed converging wick flow condenser, fabricated from a high-thermal-conductivity GRCop-42 copper alloy, for enhanced flow condensation of low surface-tension fluids using HFE-7100 dielectric as a representative working fluid. The converging wick design strategically distributes the solid–fluid interfacial area and incorporates a converging profile to offset the decline in convective effects during vapor-to-liquid transition, while maintaining mechanical robustness and long-term reliability without coatings or liquid infusion. A semi-analytical wick flow condensation model was also developed to predict thermal performance and guide optimization. Experimental and modeling results demonstrate that, at a dielectric mass flow rate of 1 g/s, the wick condenser achieved a condensation heat flux of 26.8 kW/m^2 versus 8.8 kW/m^2 for a plain condenser (204.5 % improvement). At a full condensation state with an exit vapor quality of zero, and a dielectric mass flow rate of 0.33 g/s, the heat transfer coefficient of the converging wick flow condenser increased by 111 % compared to a plain condenser. Additionally, at a saturation temperature of 29.4 °C and a coolant temperature of 20.7 °C, the performance evaluation factor was 69 % higher than its plain counterpart. While AM obviously offers the potential to create sophisticated heat transfer topologies for enhanced condensation processes, the 3D-printed condenser technology is still in its infancy. In particular, prior research on 3D-printed flow condenser technologies is mainly limited to simple heat transfer features. Exploiting the AM technology to realize condensing heat transfer features that account for variations in local thermal and fluid properties during phase change is of high interest. Addressing these research gaps offers a promising pathway for AM to unlock next-generation, highly efficient condenser technologies.

In this study, an innovative copper-based 3D-printed gradient wick flow condenser is conceptualized and examined to enhance condensation heat transfer of low-surface-tension fluids. The gradient wick flow condenser, benchmarked against a uniform wick flow condenser, incorporates spatially varying heat transfer features tailored to accommodate local variations in two-phase thermal and flow characteristics as condensation progresses. In the following sections, first, the underlying concept of the gradient wick flow condenser is discussed. Next, the design of the gradient and uniform wick flow condensers, the copper-based 3D printing process, and the flow condensation test facility are explained. Then, a semi-analytical flow condensation model is developed to better understand the thermal-fluid physics associated with the gradient and uniform wick flow condensers operating with low surface tension fluids. Finally, the experimental and modeling results of the gradient and uniform wick flow condensers are presented.

2. Concept: gradient wick flow condensers

While advanced dropwise condensation techniques have shown great promise in external condensation, their effectiveness in internal flow condensation remains limited. Moreover, the dropwise-enhanced approaches have been largely effective in the case of high surface

tension fluids, but far less effective with the widely used low surface tension fluids. Combined with the longevity concerns of many dropwise-enhancement methods, filmwise condensation remains the prevalent heat transfer mode in most industrial flow condensers employing low surface tension fluids. Novel strategies to enhance filmwise behavior in internal flow condensers could meaningfully improve the overall energy efficiency and compactness of thermal management systems.

The proposed study aims to tailor filmwise behavior of internal flow condensers by accounting for local variations in two-phase flow characteristics during the vapor-to-liquid phase transition, a strategy that is largely overlooked in the design of existing flow condensers. As shown in Fig. 1, at the heart of the proposed flow condenser, there are gradient wick structures with pore sizes varying in both longitudinal and lateral directions, offering features that not only augment but also tailor the filmwise flow condensation of low surface tension fluids. First, the pore sizes of the gradient wick structure progressively decrease in the longitudinal direction from the condenser inlet to the outlet. This provides high wick-condensate thermal conductivities at the condenser outlet, where the condensate film thickness and its associated thermal resistance are the highest. Also, this promotes capillary-assisted condensate transport and drainage along the flow direction. Additionally, the decreasing pore size gradient partially mitigates the natural decline in the convective effects as the high-velocity, vapor-rich mixture transitions to the low-velocity, liquid-rich mixture during the condensation process. Second, working in tandem with the latter feature, the trapezoidal converging profile of the condenser further compensates for the reduced convective effects due to the vapor-to-liquid transition. Sustaining convective effects, particularly at low vapor qualities near the condenser outlet, improves local condensation heat transfer coefficient and accelerates condensate removal, thereby preventing liquid accumulation. Third, the converging profile of the flow condenser offers a high solid-fluid interfacial area at the condenser inlet, where the vapor quality is high, and the mixed liquid-vapor (l-v) thermal conductivity is low. In the particular gradient wick flow condenser design examined in this study and shown in Fig. 2a, the total solid-fluid interfacial area decreases from 39.7 cm^2 at the condenser inlet to 29.3 cm^2 at the outlet per centimeter of condenser length (i.e., 39.7 to 29.2 cm^2/cm) due to the trapezoidal geometry of the condenser. Fourth, the side porous walls of each gradient wick structure offer vertically oriented menisci for both enhanced condensation and capillary wicking of the condensate from the heart of the wick structure to its outer periphery. Fifth, the lateral variation in pore size distribution creates a high-permeability core and low-permeability regions near the two side corners of the gradient wick structures. The high-permeability central core reduces viscous friction losses and thereby sustains higher vapor velocities along the flow direction at the heart of the wick. The lateral variation in pore size also enables enhanced wicking of the condensate from the heart of the gradient wick structure toward the vertically oriented side menisci. Collectively, these characteristics make the proposed gradient wick flow condenser highly effective in not only enhancing but also tailoring the filmwise heat transfer mode of internal flow condensers for extremely wetting fluids. It should be noted that the flow condensation performance of the proposed gradient wick flow condenser was benchmarked against a uniform wick flow condenser at a similar average porosity.

3. Experiment

3.1. Design of the gradient wick flow condenser

To evaluate the effectiveness of the above concept in improving the flow condensation performance of low surface tension fluids, a water-cooled gradient wick flow condenser was designed. As shown in Figs. 1 and 2, the flow condenser consists of two separate sections for the HFE-7100 dielectric and the chilled water working fluids, respectively. On the dielectric side, the gradient or uniform wick structures are fabricated. Both the gradient and uniform wick flow condensers include two triangular converging wick sections.

As shown in Fig. 2a, the gradient wick structure features a maximum pore size of 0.9 mm at the condenser inlet and a minimum pore size of 0.3 mm at the condenser outlet, which varies linearly in both longitudinal and lateral directions. The uniform wick structure incorporates a constant pore size of 0.57 mm to maintain a similar average porosity of ~73 % for both the gradient and uniform wick structures. The wall thickness is fixed at 0.3 mm. The individual wick structures are connected to a wick outlet section, as shown in Fig. 2a and b. The length, height, inlet width, and outlet width of the wick flow condenser are 102.8, 14.3, 43.6, and 13.7 mm, respectively. The chilled water side, collecting and dissipating the latent heat generated during the flow condensation process, consists of cylindrical pin fins, as depicted in Fig. 2c. A detailed simulation-based optimization study was performed to optimize the coolant-side cylindrical pin fin features, as described in our earlier publication [33]. Specifically, the effect of fin diameter varying from 1.5 to 3 mm and fin spacing varying from 1 to 3 mm was examined. The results indicated that a fin pin array with a fin diameter of 1.5 mm and a fin edge-to-edge spacing of 2 mm is optimal.

3.2. 3D printing of the gradient wick flow condenser

The proposed gradient wick flow condenser and its uniform wick counterpart were fabricated using stainless steel 17–4 pH alloy via the Selective Laser Melting (SLM) additive manufacturing technique. The stainless steel 17–4 pH alloy was chosen due to its excellent mechanical strength and corrosion resistance, particularly under extreme saline conditions, which represents one of its ultimate use cases. Both the gradient and uniform wick flow condensers were 3D-printed using the EOS M290 metal 3D printer, which utilizes a high-power 400 W Yb-fiber laser with a beam focus diameter of approximately 100 μm, enabling the production of complex geometries with high precision. The EOS M290

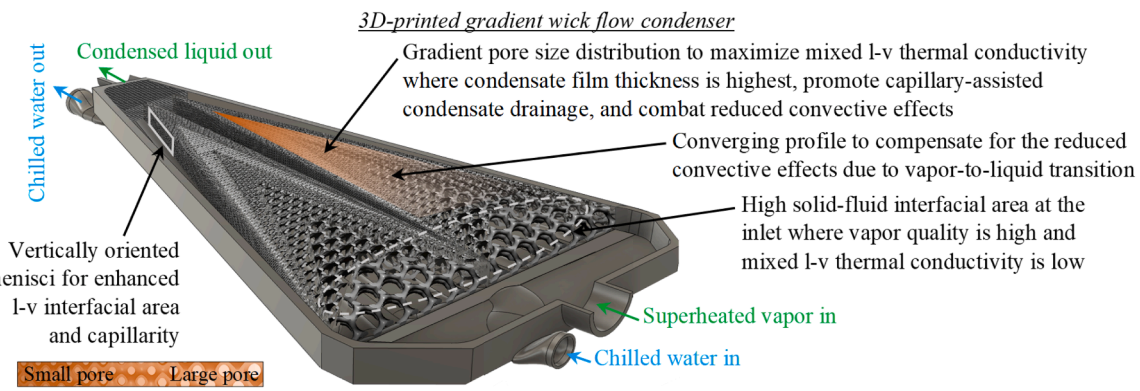

Fig. 1. Conceptual design of the proposed gradient wick flow condenser.

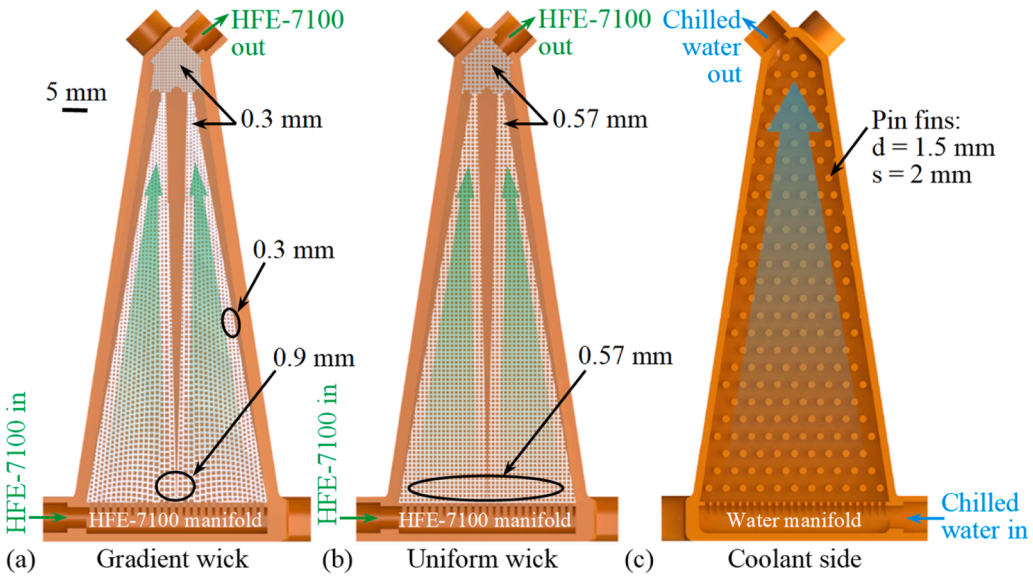

Fig. 2. Internal features of the flow condensers: (a) the gradient wick structures, (b) the uniform wick structures, and (c) the cylindrical pin fins of the chilled water side.

metal 3D printer allows a minimum pore size of 50 μm and a solid wall thickness of <150 μm with the stainless steel 17–4 pH alloy. However, both the minimum pore size and the minimum wall thickness were conservatively set to 300 μm to ensure the laser-melted pools fuse properly for high thermal conductivity and mechanical strength, as well as facilitating the proper removal of loose metal powder trapped inside 3D-printed condensers after printing.

Fig. 3a shows an image of the 3D-printed gradient wick flow condenser made of the stainless steel 17–4 pH alloy. Fig. 3b and c show X-ray images of the 3D-printed gradient and uniform wick structures, highlighting both the wick and pin fin features. Given the presence of fine wick features on the dielectric side, the print orientation was carefully optimized to ensure structural fidelity. As such, a build angle of 45° was selected to initiate the print from the wider base of the condenser and progress toward the narrower end, facilitating structural support and minimizing deformation during the print process. Post-processing involved a multi-step powder removal procedure to ensure full clearance of residual powders trapped within the wick structures. Initially, the trapped loose powders were removed using a combination of a dry air stream and mechanical vibration/sonication. Then, the printed condensers were immersed in an isopropyl alcohol (IPA) solution and subjected to high-frequency sound waves to effectively dislodge any remaining trapped powders. Subsequently, the IPA solution was pumped through the wick network to flush out any remaining particulates. The weights of the printed condensers were recorded before and after each cleaning step to evaluate their effectiveness in removing trapped loose powder. The above cleaning process was repeated as necessary. Furthermore, preliminary pressure proof testing indicated the proposed 3D-printed condenser can withstand internal pressures exceeding 60 bar, well above the operating pressures of commonly used refrigerants.

3.3. Flow condensation test facility

A flow condensation test facility was developed to experimentally evaluate the flow condensation performance of the gradient wick flow condenser for low surface tension fluids. The flow condensation experiments were conducted with the HFE-7100 dielectric fluid as a

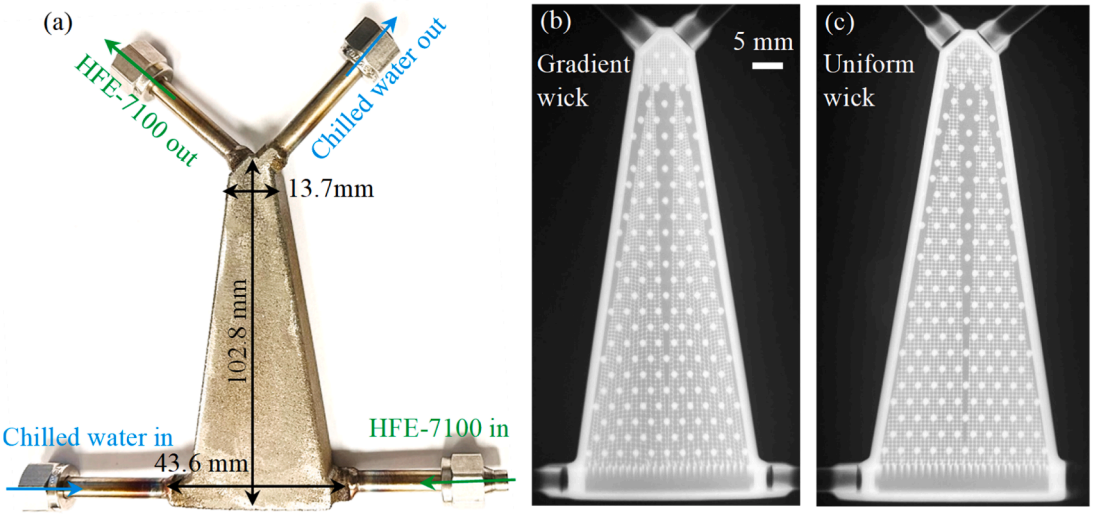

Fig. 3. (a) An image of the 3D-printed gradient wick structure with brazed connection tubes. (b and c) X-ray images of the 3D-printed gradient and uniform wick structures, highlighting both the wick and pin fin features.

representative low surface tension fluid. The important thermophysical properties of HFE-7100 and their value ranges, obtained from Engineering Equation Solver (EES), are included in Table 1. Fig. 4 shows a schematic of the flow condensation test facility consisting of an HFE-7100 flow loop and a chilled water loop. The test facility includes a dielectric reservoir, a submersible pump, an inline heater, the 3D-printed flow condenser, and a chiller. To eliminate the presence of parasitic non-condensable gases, the dielectric flow loop was kept under vacuum using a vacuum pump (Model: ScrollVac10+). A leak test was performed prior to the condensation experiments to ensure that the dielectric loop was hermetically sealed. An ultrasonic mass flow meter with an accuracy of 1 % (Model: Keyence FD-XS1) was employed to measure the HFE-7100 mass flow rate. The ultrasonic flow meter was calibrated against a Coriolis flow meter (Model: Micro Motion ELITE CMF025H Coriolis Flow Meter, Emerson Electric Co., with an accuracy of 0.05 % RD) before the experiments. An in-line heater was used to maintain a superheat of ~ 2.5 °C for the HFE-7100 fluid at the condenser inlet. Additionally, the inlet and outlet pressures were measured using pressure transducers with an accuracy of 0.25 % reading (Model: Setra 730 G). Furthermore, using a chiller (Model: ThermoChill I), a chilled water stream was circulated through the coolant side of the condenser. Different subcooling levels were achieved by adjusting the cold water inlet temperature. All temperature measurements were obtained using T-type thermocouples (Model: Omega TMTSS-062 U) that were calibrated against an ultra-precision Pt100 RTD sensor with an accuracy of ±0.2 °C. The mass flow rate of the water was determined using a mass flow meter. The pressure and temperature data were continuously monitored and recorded at a frequency of 1 Hz by a data acquisition system (Model: KEYSIGHT 34972A). To minimize heat gain, an insulation casing made of polytetrafluoroethylene (PTFE) enclosed the outer body of the 3D-printed flow condenser. Before the condensation tests, a dry test was performed to measure the heat gain from the ambient at different condenser body temperatures. It should be noted that a counter-flow configuration is the most commonly used flow arrangement. However, due to the trapezoidal geometry of the proposed condenser, the heat transfer area is largest at the wider inlet end. Consequently, it is advantageous to maximize the temperature difference on the wider end of the condenser, which suggests a co-current flow configuration. This design choice was further validated by preliminary comparative tests between counter-flow and co-current operation, which indicated improved thermal performance for the co-current configuration in the present geometry.

3.4. Data reduction and uncertainty analysis

The total cooling rate exchanged by the water flow stream ($\dot{Q}_{total}$) is calculated as follows:

$$\dot{Q}_{total} = \dot{m}_w c_{p,w}\left(T_{w,out} - T_{w,in}\right) \tag{1}$$

where $\dot{m}_w$, $c_{p,w}$, $T_{w,in}$, and $T_{w,out}$ are the mass flow rate, specific heat, and inlet/outlet temperatures of water, respectively. Then, the net heat transfer rate ($\dot{Q}_{net}$) and condensation heat flux (q'') considering the heat gain ($\dot{Q}_{gain}$) are calculated as follows:

Table 1
Properties of HFE-7100 working fluid.

Property [unit]	Temperature range	Value range
Density of liquid [kg/m^3]	18–30 [°C]	1504–1534
Density of vapor [kg/m^3]		3.02–4.2
Viscosity [cP]		0.62–0.76
Thermal conductivity [W/m-K]		0.068–0.07
Surface tension [mN/m]		12.35–13.45
Specific heat [J/kg-K]		1169–1193
Latent heat of evaporation [kJ/kg]		123–127.3

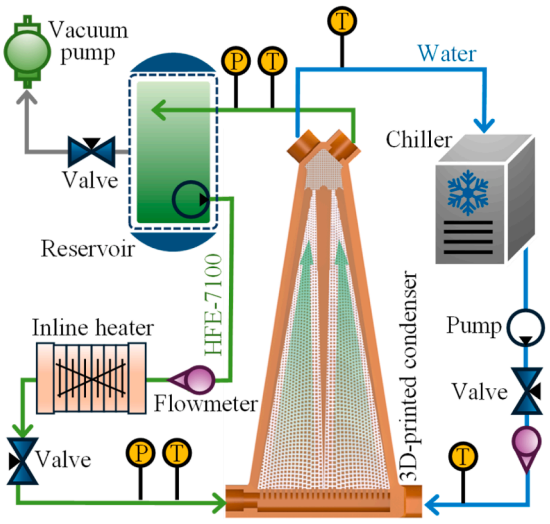

Fig. 4. A schematic of the flow condensation test facility.

$$\dot{Q}_{net} = \dot{Q}_{total} - \dot{Q}_{gain} \tag{2}$$

$$q'' = \dot{Q}_{net}/A_{proj} \tag{3}$$

where A_{proj} is the projected surface area. The dielectric-side condensation heat transfer coefficient (HTC_{die}) is calculated as follows:

$$HTC_{dei} = \frac{q''}{T_{sat,die,ave} - T_{wall-die}} \tag{4}$$

where $T_{sat,die,ave}$ is the average dielectric saturation temperature corresponding to the dielectric inlet and outlet pressures. Also, $T_{wall-die}$, the average temperature at the wall-dielectric interface, is calculated as follows:

$$T_{wall-die} = 0.5\ \left(T_{w,in} + T_{w,out}\right) + \frac{\dot{Q}_{net}}{A_{proj}}\left(\frac{t}{k_s} + \frac{1}{HTC_w}\right) \tag{5}$$

where t is the wall thickness and k_s is the material thermal conductivity. Using a separate test setup shown in Fig. 5a, the water-side HTC, HTC_w, is calculated as follows:

$$HTC_w = \frac{\dot{Q}_{w,net}}{A_{proj}\left(T_{wall-water} - 0.5\ \left(T_{w,in} + T_{w,out}\right)\right)} \tag{6}$$

where $\dot{Q}_{w,net}$ is the net water heat transfer rate in the test setup shown in Fig. 5a. Also, $T_{wall-water}$, the average temperature at the wall-water interface in Fig. 5a, is calculated as follows:

$$T_{wall-water} = T_{wall-TIM,ave} + \frac{\dot{Q}_{net} t}{k_s\ A_{proj}} \tag{7}$$

where $T_{wall-TIM,ave}$ is the average temperature of the interface between the wall and the thermal interface material (TIM), which is directly measured as shown in Fig. 5a. Additionally, the dielectric exit vapor quality can be calculated as follows:

$$x_e = 1 - \left(\frac{\dot{m}_{cond}}{\dot{m}_{dei}}\right) \tag{8}$$

where, $\dot{m}_{cond}$ and $\dot{m}_{die}$ are the condensate and dielectric mass flow rates, respectively. The condensate mass flow rate is calculated as follows:

$$\dot{m}_{cond} = \left(\dot{Q}_{net} - \left(\dot{m}_{dei} c_{p,dei} \Delta T_{\sup,inlet}\right)\right)/h_{f\,g} \tag{9}$$

where $\Delta T_{sup,inlet}$ and h_{fg} are the dielectric superheat temperature at the

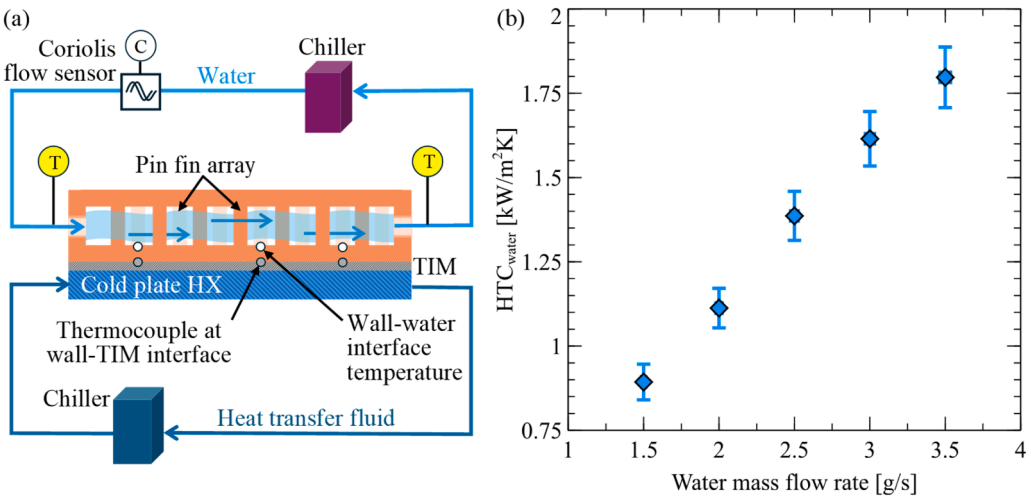

Fig. 5. (a) A schematic of the test facility to estimate the water-side HTC and (b) water-side HTC as a function of water mass flow rate.

condenser inlet and the dielectric latent heat of evaporation estimated at the dielectric average saturation temperature, respectively. Furthermore, the uncertainties associated with all important parameters of interest are calculated as follows and presented as error bars in Figs. 5 and 7–10.

$$\delta\dot{Q}_{net} = \sqrt{\left(c_{p,w}\ \Delta T_w\ \delta\dot{m}_w\right)^2 + \left(\dot{m}_w\ c_{p,w}\ \delta\Delta T_w\right)^2 + \left(\delta\dot{Q}_{gain}\right)^2} \tag{10}$$

$$\delta HTC_{dei} \Big/ HTC_{dei} = \sqrt{\left(\delta\dot{Q}_{net}/\dot{Q}_{net}\right)^2 + \left(\delta\Delta T_a/\Delta T_a\right)^2 + \left(\delta A_{proj}/A_{proj}\right)^2} \tag{11}$$

$$\delta HTC_{w} \Big/ HTC_{w} = \sqrt{\left(\delta\dot{Q}_{w,net}/\dot{Q}_{w,net}\right)^2 + \left(\delta\Delta T_b/\Delta T_b\right)^2 + \left(\delta A_{proj}/A_{proj}\right)^2} \tag{12}$$

$$\delta x_e \Big/ x_e = \sqrt{\left(\delta\dot{m}_{dei}/\dot{m}_{dei}\right)^2 + \left(\delta\dot{m}_{cond}/\dot{m}_{cond}\right)^2} \tag{13}$$

where ΔT_a is $\left(T_{sat,die,ave} - T_{wall-die}\right)$ and ΔT_b is $\left(T_{wall-water} - 0.5\left(T_{w,in} + T_{w,out}\right)\right)$.

3.5. Water-side heat transfer coefficient

Fig. 5a shows a schematic of the experimental test setup employed to estimate the water-side HTC. The water test section, consisting of the pin-fin array, was attached to a cold-plate heat exchanger using a TIM. As shown in Fig. 5a, three T-type thermocouples (Model: Omega TMTSS-062 U) with an accuracy of ±0.2 °C were inserted at the interface between the test section and the TIM. The test setup primarily comprised two independent fluid loops: one loop circulated water through the test section, and the other circulated a heat transfer fluid through a bottom cold-plate heat exchanger. Two additional T-type thermocouples (Model: Omega TMTSS-062 U) with an accuracy of ±0.2 °C were used to measure the inlet and outlet water temperatures. A criolisis flow meter (Model: Micro Motion ELITE CMF025H Coriolis Flow Meter, Emerson Electric Co., with an accuracy of 0.05 % RD) was employed to measure the water mass flow rate. Fig. 5b shows the water-side HTC as a function of the water mass flow rate. As shown in Fig. 5b, the water-side HTC increases with the water mass flow rate due to enhanced convective heat transfer effect at higher flow rates. In the following condensation experiments, the water mass flow rate was maintained at a constant mass flow rate of 2.5 g/s.

4. Gradient wick flow condensation model for low surface tension fluids

Here, a semi-analytical model is proposed to provide insight into the local physics of the gradient wick flow condensation process of low surface tension fluids. The primary objective of this model is to serve as a physics-based interpretive tool that enables examination of local quantities such as spatial variations in condensate film thickness, HTC, and local heat flux that are challenging to directly measure using the current flow condensation test setup. The present modeling framework for gradient wick flow condensers expands upon our prior research [32], which established a flow condensation model for uniform wick flow condensers. Here, a concise overview of the uniform wick flow condensation model is first provided, and then its extension to accommodate gradient wick structures is discussed. The model considers the following assumptions and limitations:

- The flow regime of the condensate film is steady-state and laminar.
- Saturated pure vapor with a uniform saturation temperature enters the condenser.
- Thermophysical properties of HFE-7100, as listed in Table 1, are evaluated at the relevant operating temperatures and pressures.
- Dielectric saturation temperature linearly changes from inlet to outlet.
- The wick structure in the vapor domain is at T_{sat} and has a negligible fin efficiency due to a high HTC associated with the condensation process.
- Vapor shear forces dominate capillary forces due to a low surface tension fluid being condensed.
- Subcooling of the condensate film is neglected.

Fig. 6 shows a schematic of a saturated vapor stream flowing through a gradient wick structure. As shown, the thickness of the condensate film increases along the flow direction. Since the wick-condensate thermal conductivity is higher than that of a pure condensate film, the heat released during the condensation process is effectively dissipated. The zoomed-in view in Fig. 6 shows force balances on an elemental condensate volume. The main forces are the pressure gradient in the condensate film, the viscous force, and the interfacial shear force. The force balance on the control volume shown can be written as follows:

$$\tau_v dz + dP_l(\delta - y) = \mu_l(du_l\,/\,dy)\ \gamma\ dz \tag{14}$$

where μ_l and τ_v are the liquid viscosity and the interfacial shear stress. Additionally, the following parameters are considered for a two-phase fluid and a porous structure:

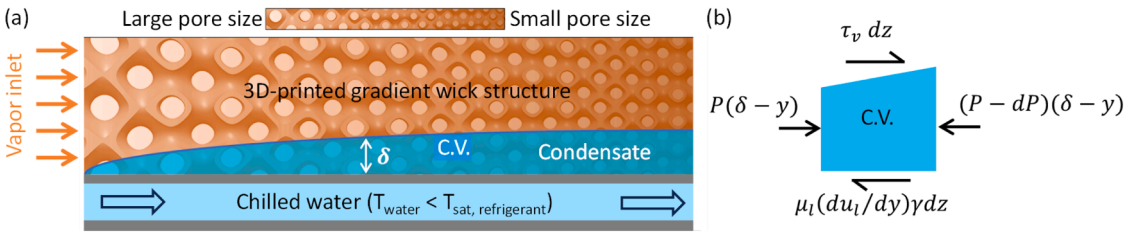

Fig. 6. (a) A schematic of the gradient wick flow condenser and (b) force balance on an elemental volume of the condensate.

$$x = \dot{m}_v / \dot{m}_{total} \tag{15}$$

$$\gamma = A_{actual} / A_{proj} \tag{16}$$

$$\varepsilon = A_{c,f} / A_{c,total} \tag{17}$$

$$\alpha = A_{c,v} / A_{c,f} \tag{18}$$

where x, γ, ε, and α are the vapor quality of the two-phase mixture, local enhanced surface area by the gradient wick structure, local porosity of the gradient wick structure, and local void fraction. Also, $\dot{m}_v$, $\dot{m}_{toal}$, A_{actual}, A_{proj}, $A_{c,f}$, $A_{c,total}$, and $A_{c,v}$ are the vapor mass flow rate, the total dielectric mass flow rate, the actual heat transfer area, the projected surface area, the fluid (vapor and liquid) cross-sectional area (subtracting solid area), the total (vapor, liquid, and solid) cross-sectional area, and the vapor cross-sectional area, respectively. Integrating Eq. (14) twice and then rearranging the equation with the condensate mass flow rate considered, the following relationship is derived:

$$d\delta / d\dot{m}_l = \gamma\, \mu_l \,/\, \left[\rho_l\, \varepsilon\, W\, (dP/dz)_l\, \delta^2 + \tau_v\, \rho_l\, \varepsilon\, W\, \delta\right] \tag{19}$$

where W is the width of the wick structure as follows:

$$W(z) = W_{max} - \frac{W_{max} - W_{min}}{L} \times z \tag{20}$$

where W_{max} W_{min}, and L are the maximum/minimum width and length of the wick flow condenser. Next, considering the mass and energy balances for the elemental condensate volume, the latent heat of condensation is equal to the wall heat flux, and the variation of condensed liquid mass flow rate can be calculated from:

$$d\dot{m}_l / dz = W\, q'' \,/\, h_{fg} = W\, h(y,z)\, \Delta T \,/\, h_{fg} = W\, k_{wc}\, \Delta T \,/\, \delta h_{fg} \tag{21}$$

where $k_{wc} = C_{th} C_d (\varepsilon k_l + (1 - \varepsilon) k_s)$ is the effective wick-condensate thermal conductivity. C_{th} and C_d are the thermohydraulic and design-dependent flow correction coefficients, respectively, and are determined empirically from the experimental results. C_{th} accounts for the thermohydraulic parameters that affect the thermal efficiency of a wick structure, including fin efficiency influenced by the effectiveness of the cooling temperature potential and convective flow effects within the condensate film. C_d accounts for the effect of the wick design on the flow regime at a fixed thermohydraulic parameter set. $\Delta T = T_{sat} - T_w$ is the cooling temperature potential. By multiplying Eq. (19) and Eq. 21, the derivative of liquid film thickness with respect to the condenser length is determined from the following equation:

$$d\delta / dz = \gamma\, \mu_l\, k_{wc}\, \Delta T \,/\, \left[\rho_l\, h_{fg}\, \varepsilon\, (dP/dz)_l\, \delta^3 + \tau_v\, \rho_l\, \varepsilon\, h_{fg}\, \delta^2\right] \tag{22}$$

where τ_v is the interfacial shear stress, τ_v, and can be expressed as a function of an interfacial friction factor [32]. Solving Eq. 22, the variation of the condensate film thickness can be obtained. While in our previous study of the uniform wick flow condenser, the variation of condensate film thickness was only considered along the longitudinal condenser direction (i.e., z), in the case of the gradient wick flow condenser, it will vary along the lateral condenser direction (i.e., y) as well. This effect can be captured by varying the porosity along length and width as follows:

$$\varepsilon(y,z) = \varepsilon_{max} + \left(\frac{\varepsilon_{min} - \varepsilon_{max}}{L}\right) z \;-\; \left(\frac{\varepsilon_{min} - \varepsilon_{max}}{W}\right) y \tag{23}$$

where ε_{min} and ε_{max} are the minimum (i.e., corresponding to the minimum pore size) and maximum porosity (i.e., corresponding to the maximum pore size), respectively. Once the condensate film thickness, $\delta(y,z)$, is calculated as a function of y (i.e., lateral condenser direction) and z (i.e., longitudinal condenser direction), the local heat transfer coefficient, $HTC(y,z)$, and the local heat flux, $q''(y,z)$, can be calculated as follows:

$$HTC(y,z) = C_{th} C_d (\varepsilon k_l + (1 - \varepsilon) k_s) / \delta(y,z) \tag{24}$$

$$q''(y,z) = h(y,z)\; \Delta T \tag{25}$$

5. Results and discussion

5.1. Effect of cooling water temperature on the gradient wick flow condensation

First, a comparative analysis was conducted to evaluate the flow condensation performance of the gradient wick flow condenser against its uniform counterpart at different chilled water temperatures and a constant HFE-7100 mass flow rate of 0.6 g/s. Fig. 7a shows the variations of the condensation heat flux as a function of the cooling temperature potential, defined as the difference between the HFE-7100 saturation and chilled water temperatures. As shown, the condensation heat flux increases at higher cooling temperature potentials (i.e., lower water temperatures) for both the gradient and uniform wick flow condensers. At a fixed HFE-7100 saturation temperature and vapor pressure, a lower cooling water temperature reduces the equilibrium vapor pressure at the condensing solid surfaces, thereby increasing the vapor pressure potential driving the condensation process. More importantly, the gradient wick flow condenser demonstrates a higher heat flux in comparison to its uniform counterpart at a given cooling temperature potential. For instance, at a cooling temperature potential of 14 °C, the gradient wick flow condenser demonstrates a 37 % enhancement in the condensation heat flux compared with its uniform counterpart (i.e., heat flux of approximately 10.3 versus 7.5 kW/m^2). This is mainly attributed to the pore size distribution of the gradient wick flow condenser that progressively decreases in both longitudinal and lateral directions to account for local variations in two-phase flow characteristics during the vapor-to-liquid phase transition.

Fig. 7b shows that the exit vapor quality decreases with the cooling temperature potential. This is expected as the cooling temperature potential serves as the main driving force for the condensation process. Also, the exit vapor quality of the gradient wick flow condenser is lower than that of the uniform wick flow condenser at a similar cooling temperature potential. This is attributed to the higher condensation heat transfer rate of the gradient wick structure in comparison to its uniform counterpart. Additionally, the semi-analytical flow condensation model accurately predicts the experimentally measured condensation heat flux and exit vapor quality for both gradient and uniform wick flow

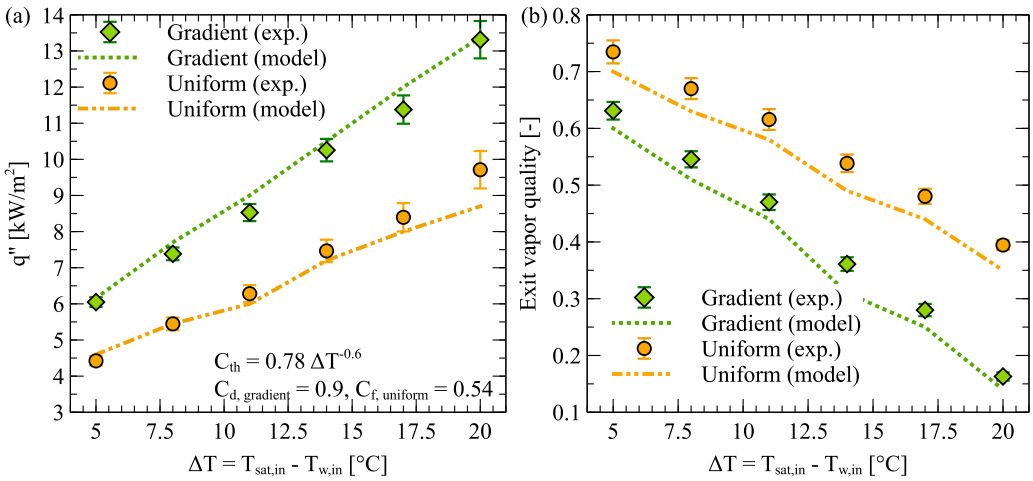

Fig. 7. Effect of cooling temperature potential on (a) condensation heat flux and (b) exit vapor quality of gradient and uniform wick flow condensers at a constant HFE-7100 mass flow rate of 0.6 g/s.

condensers with a maximum deviation of <7 %. Comparing the experimental and modeling results reveals that, at a fixed dielectric mass flow rate, the thermohydraulic correction coefficient (C_{th}) depends on the cooling temperature potential, as it affects the thermal efficiency of the wick structure and varies as $C_{th} = 0.78\ \Delta T^{-0.6}$ with ΔT being in degrees Celsius. Furthermore, the flow correction coefficients (C_d), which considers the design-flow regime dependency, are determined to be 0.9 and 0.54 for the gradient and uniform wick flow condensers, respectively.

Next, the HTC and the two-phase pressure drop penalty of the gradient and the uniform wick flow condensers are compared. Fig. 8a shows the variations of the HTC versus the exit vapor quality at a constant HFE-7100 mass flow rate of 0.6 g/s. As shown, the HTC declines as the exit vapor quality decreases (i.e., more condensation). This is attributed to (i) a change in the flow regime at low exit vapor qualities, resulting in diminished convective effects, and (ii) the formation of a thicker condensate film at lower exit vapor qualities, both of which reduce the flow condensation HTC. However, it is important to highlight that, at low exit vapor qualities (i.e., a highly condensed flow regime), the gradient wick flow condenser maintains a significantly higher HTC compared with the uniform wick flow condenser. For instance, at an exit vapor quality of ~0.38 and a fixed dielectric mass flow rate of 0.6 g/s, the gradient wick flow condenser demonstrates a 67 % improvement in the flow condensation HTC compared to its uniform counterpart (i.e., a HTC of 0.97 versus 0.58 kW/m^2-K). This highlights the importance of the pore size distribution, particularly at low exit vapor qualities, where the convective effects are weakest, and the condensate film thickness is the highest.

Fig. 8b demonstrates that the two-phase pressure drop penalty decreases with an increase in the cooling temperature potential. This is because, at higher cooling temperature potentials, the exit vapor quality decreases, resulting in reduced convective effects and their associated acceleration pressure drop term. Also, the results indicate that the pressure drop penalty of the gradient wick flow condenser is higher than that of the uniform wick flow condenser. This is primarily attributed to the narrow pore size distribution of the gradient wick flow condenser toward its outlet. The finding highlights the need for further optimization of the gradient wick flow condenser to reduce its pressure drop without significantly compromising its flow condensation performance. In fact, it was determined that the small pore size of the outlet wick section in the gradient wick condenser contributes most to the total pressure drop penalty. As such, future studies will focus on optimizing the pore size of the outlet wick section of the gradient wick topology.

5.2. *Effect of dielectric mass flow rate*

Fig. 9a shows the effect of the dielectric mass flow rate on the condensation heat flux. The coolant water temperature was adjusted to have an almost constant average cooling temperature potential of 5 ±

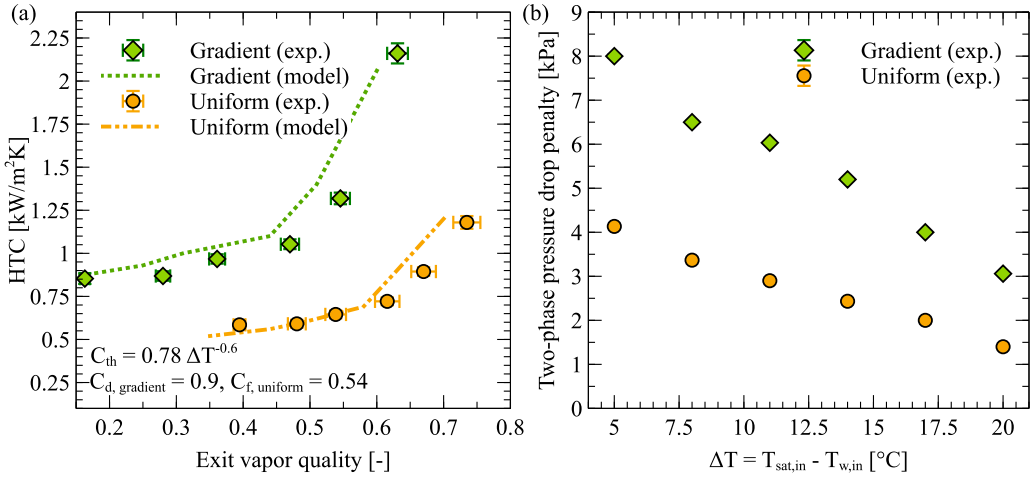

Fig. 8. Variations of (a) HTC as a function of exit vapor quality and (b) two-phase pressure drop penalty versus cooling temperature potential of gradient and uniform wick flow condensers at a constant HFE-7100 mass flow rate of 0.6 g/s.

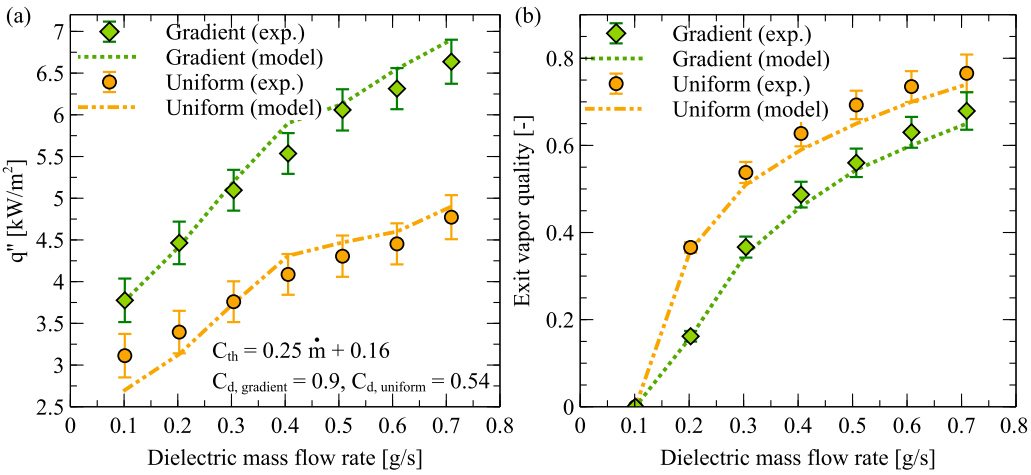

Fig. 9. Effect of dielectric mass flow rate on (a) condensation heat flux and (b) exit vapor quality of gradient and uniform wick flow condensers at a constant cooling temperature potential of 5 °C.

0.25 °C at different test conditions. In the present study, the dielectric mass flow rates vary from 0.1 to 0.7 g/s, corresponding to mid-length mass fluxes of 2.4–17 kg/m^2-s. It should be noted that the local mass flux varies along the flow direction due to the trapezoidal geometry of the proposed wick flow condenser. Accordingly, the reported mass flux values are calculated using the average cross-sectional flow area at the condenser mid-length and accounting for an average wick porosity of 73 %. As expected, the condensation heat flux increases with the dielectric mass flow rate, due to the enhanced convective heat transfer effects. Also, the gradient wick flow condenser demonstrates a higher condensation heat flux compared with the uniform wick flow condenser for all mass flow rates tested. For instance, at a mass flow rate of 0.4 g/s, the gradient wick flow condenser demonstrates a 35 % improvement in the condensation heat flux of the HFE-7100 working fluid compared to its uniform counterpart (i.e., 5.5 versus 4 kW/m^2). This could be largely attributed to the progressively narrow pore sizes of the gradient wick structures at low vapor qualities, resulting in higher convective effects and effective wick-condensate thermal conductivity. In addition, as shown in Fig. 9a, the condensation heat flux tends to plateau at higher dielectric flow rates, as the thermal resistance on the water side becomes increasingly dominant.

Fig. 9b shows the effect of the dielectric mass flow rate on the exit vapor quality of the gradient and uniform wick flow condensers at a constant cooling temperature potential of 5 °C. As shown, the exit vapor quality increases at higher dielectric mass flow rates. This indicates that the effect of the added sensible heat on the exit vapor quality dominates over the effect of the augmented HTC at high dielectric mass flow rates. At a fixed dielectric mass flow rate, the exit vapor quality of the gradient wick flow condenser is lower than that of its uniform counterpart due to the higher heat flux and HTC of the gradient wick structure. Additionally, at a constant cooling temperature potential, a close match between the semi-analytical flow condensation model and the experimentally measured condensation heat flux and exit vapor quality of the gradient and uniform wick flow condensers was observed with a maximum deviation of <5 %. A comparison between the experimental and modeling results indicates that, at a fixed cooling temperature potential, the thermohydraulic correction coefficient depends on the dielectric mass flow rate as $C_{th} = 0.25\,\dot{m} + 0.16$. Furthermore, the design correction coefficients of the gradient and uniform wick flow condensers remain the same at 0.9 and 0.54, respectively.

Fig. 10a shows the variations of the HTC versus exit vapor quality at a constant cooling temperature potential of 5 °C. Similar to Fig. 8a (in which the dielectric mass flow rate was constant), at a fixed cooling temperature potential, the HTC decreases at low vapor qualities due to the reduced convective effects and the formation of thick condensate films. At a full condensate state (i.e., an exit vapor quality of 0) and a fixed cooling temperature potential of 5 °C, the gradient wick flow condenser exhibits a 26 % higher condensation heat transfer coefficient

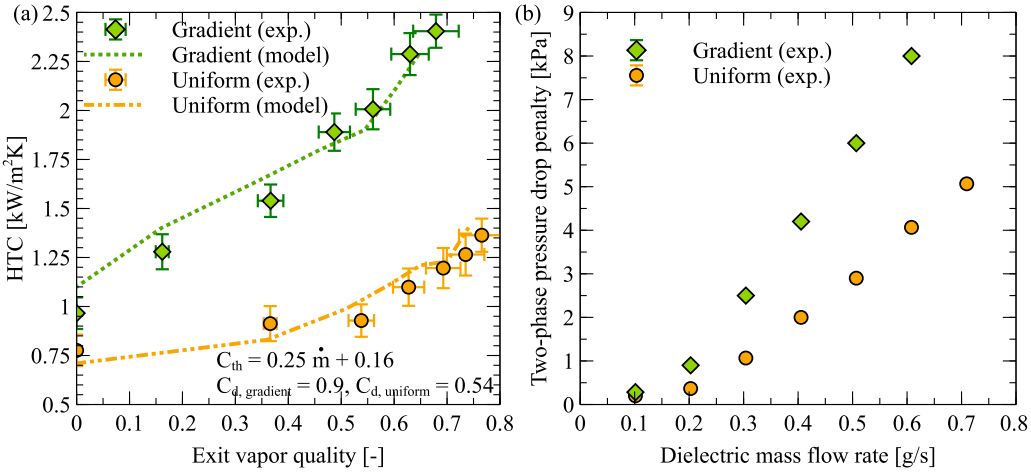

Fig. 10. Variations of (a) HTC as a function of exit vapor quality and (b) two-phase pressure drop penalty versus dielectric mass flow rate of gradient and uniform wick flow condensers at a constant cooling temperature potential of 5 °C.

than its uniform counterpart (i.e., 0.97 versus 0.77 kW/m^2-K). Fig. 10b shows the variations of the two-phase pressure drop penalty as a function of the dielectric mass flow rate at a constant cooling temperature potential of 5 °C. An increase in the mass flow rate intensifies the frictional pressure drop losses, leading to a corresponding rise in the pressure drop. The two-phase pressure drop penalty of the gradient wick flow condenser is higher than that of its uniform counterpart due to its progressively narrowing pore size distribution. This finding emphasizes that future research efforts should focus on optimizing the pore size distribution of the gradient wick flow condenser, balancing enhanced condensation heat transfer with the associated pressure drop penalty.

Next, the condensation performance of the proposed wick flow condensers is compared against state-of-the-art condensers [31,34,35], as shown in Fig. 11, highlighting the normalized power density versus the normalized pumping power. To facilitate a fair comparison, the power density is defined as the ratio of the condensation heat transfer rate to the condenser volume. Also, the comparison is limited to studies that employ condenser materials with a thermal conductivity comparable to that of the stainless steel used in the present study. Additionally, to account for variations in working fluid, the power density is normalized by the latent heat of condensation. Furthermore, the normalized pumping power is defined as the ratio of the total pumping power, comprising contributions from both the coolant and dielectric fluids, to the condensation heat transfer rate. As shown in Fig. 11, at a given normalized pumping power of ~1.3 × 10^{-6}, the gradient wick flow condenser demonstrates a 21 % higher normalized power density compared to its uniform counterpart (i.e., 3.5 versus 2.9 kg/m^3-s) at a full condensation state. Also, the condensation performance of both the gradient and uniform wick flow condensers outperforms the performance of the condensers developed by Zhang et al. [34] and Longo et al. [35], achieving comparable power density while requiring an order of magnitude lower pumping power. For instance, at a full condensation state, Zhang et al. [34] showed a maximum normalized power density of approximately 3.5 kg/m^3-s at a corresponding normalized pumping power of 0.004. In contrast, the gradient wick structure achieves a similar normalized power density of 3.5 kg/m^3-s at a drastically lower normalized pumping power of ~1.3 × 10^{-6}, demonstrating a superior overall condensation performance. While the condensers offered by Swep (brazed-plate, Models: B15THx16/1P and B10THx16/1P) exhibit a higher normalized power density compared to the wick flow condensers of the present study, it does so at the expense of significantly greater normalized pumping powers, as evident from Fig. 11.

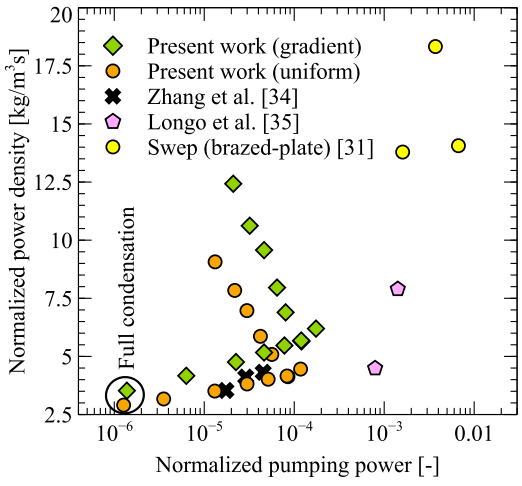

Fig. 11. A comparison of the condensation performance of the proposed 3D-printed gradient/uniform wick flow condensers against state-of-the-art condensers.

5.3. Model insights

Upon validating the semi-analytical model, it was employed to study the detailed physics of the gradient and uniform wick flow condensation process. Fig. 12a shows contours of the local condensate film thickness, *δ(y,z)*, for the gradient and uniform wick flow condensers at a dielectric mass flow rate of 0.7 g/s and a cooling temperature potential of 20 °C. The results are shown for half of the symmetric domain. The film thickness at the upstream edge of the wick flow condensers was experimentally measured in a separate experiment using a confocal displacement sensor with an accuracy of ±0.41 μm (Model: Keyence CL-P015). As shown, the condensate film gradually increases along the condenser length as the vapor quality decreases during the vapor-to-liquid transition process. The gradient wick flow condenser demonstrates a more pronounced increase in the condensate film thickness due to its superior condensation performance compared to its uniform counterpart. Notably, the condensate film thickness of the gradient wick flow condenser varies in both longitudinal and lateral directions, owing to its spatially graded pore distribution influencing the local condensation rate. In contrast, the condensate film thickness of the uniform wick flow condenser primarily varies in the longitudinal direction. Overall, the condensate film thickness contours indicate that the condensate film thickness increases as the pore size decreases due to an intensified local condensation rate. Fig. 12b shows contours of the local heat transfer coefficient, *HTC(y,z)*, for the gradient and uniform wick flow condensers at a dielectric mass flow rate of 0.7 g/s and a cooling temperature potential of 15 °C. As shown, the gradient wick flow condenser exhibits a higher HTC compared to its uniform counterpart under identical operating conditions. This enhancement primarily stems from the elevated effective thermal conductivity of the gradient wick structure at low vapor qualities near the condenser outlet, where the high thermal resistance of a thick condensate film would otherwise degrade the condensation rate. It is also evident that the gradient wick flow condenser offers a high heat transfer coefficient anywhere that the pore size of the wick structure is small. Interestingly, although the gradient wick flow condenser has a large pore size at the inlet of the condenser, a thin condensate film at the condenser upstream results in moderately high HTCs. Additionally, the contours indicate that the HTC of the plain sections is minimum, for both the gradient and uniform wick flow condensers, due to the high thermal resistance associated with the condensate film in the absence of the wick structure.

Fig. 13 shows the cross-sectional average condensate film thickness, condensation heat flux, and HTC for both the gradient and uniform wick flow condensers. The dielectric mass flow rate and the cooling temperature potential are fixed at 0.7 g/s and 15 °C, respectively. Fig. 13 sheds light on how the two pore size distribution profiles associated with gradient and uniform wick structures affect key performance metrics along the condenser length. As expected, the condensate film thickness increases along the condenser length for both the gradient and uniform wick flow condensers. At the condenser outlet, the average condensate film thickness of the gradient wick flow condenser exceeds that of the uniform wick flow condenser due to its smaller pore size distribution. More importantly, the average condensation heat flux and HTC of the gradient wick flow condenser increase along the condenser length (green curves in Figs. 13b and 13c) despite the condensate film thickening. This is in sharp contrast to conventional condenser designs, including the uniform wick flow condenser, which demonstrate a decline in both metrics along the condenser length as the condensate film thickens (orange curves in Figs. 13b and 13c). As mentioned before, the total solid-fluid interfacial area of the gradient wick flow condenser decreases from 39.7 to 29.3 cm^2/cm from the condenser inlet to outlet due to its trapezoidal geometry. Despite this reduction in the interfacial area, the increase in the average condensation heat flux and HTC of the gradient wick flow condenser along the condenser length indicates that the solid-fluid interfacial area is not the dominant enhancement mechanism. Instead, the performance improvement is primarily attributed to

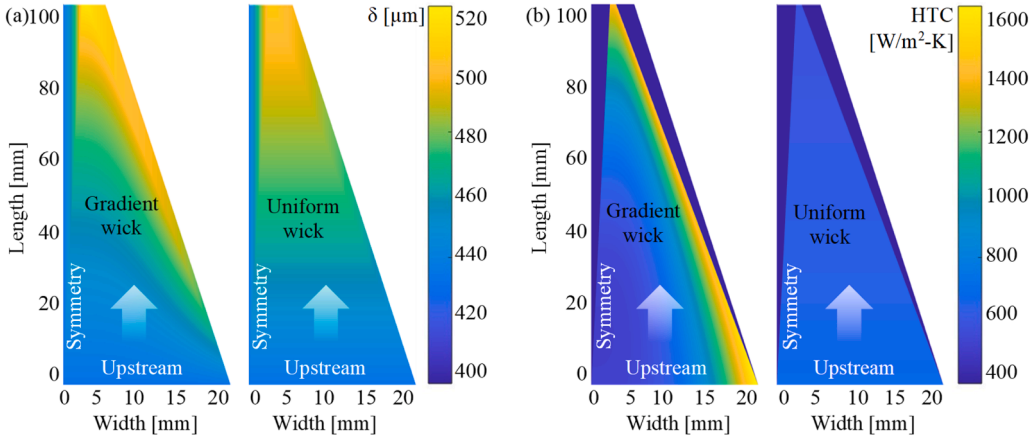

Fig. 12. Contours of the (a) local condensate film thickness, $\delta(y,z)$, and (b) local heat transfer coefficient, $HTC(y,z)$, for the gradient and uniform wick flow condensers at a dielectric mass flow rate of 0.7 g/s and a cooling temperature potential of 15 °C. The results are shown for half of the symmetric domain.

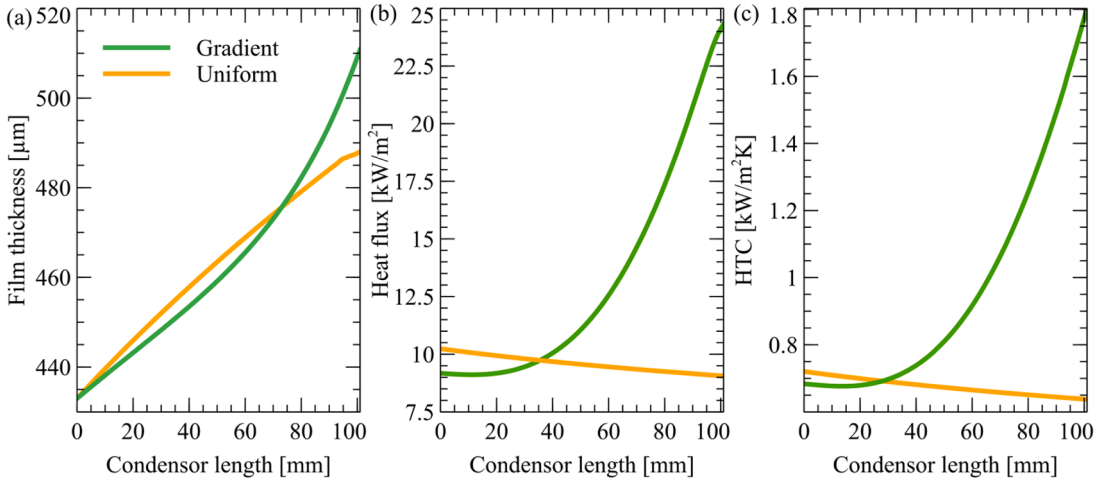

Fig. 13. Variations of the cross-sectional average (a) condensate film thickness, (b) condensation heat flux, and (c) heat transfer coefficient along the condenser length at a dielectric mass flow rate of 0.7 g/s and a cooling temperature potential of 15 °C.

(i) the enhanced effective wick-condensate thermal conductivity at the outlet of the gradient wick flow condenser, where the condensate film thickness and its associated thermal resistance are the highest, and (ii) the increased convective effects near the outlet of the gradient wick flow condenser due to the decreasing pore size gradient. It should be noted that the initial decline in the average condensation heat flux and HTC of the gradient wick flow condenser (green curves in Figs. 13b and 13c) indicates that, in this inlet region, the negative impact of the condensate film thickening outweighs the positive effect of the progressively narrowing pore size distribution. This observation suggests that the pore size distribution of the gradient wick flow condenser could be further optimized to achieve a monotonically increasing average condensation heat flux and HTC along the entire condenser length. Furthermore, the average condensation heat flux and HTC of the gradient wick flow condenser are initially lower at the condenser inlet but become higher at the condenser outlet compared to those of the uniform wick flow condenser. This behavior arises because the gradient wick flow condenser consists of large pores (900 μm) at the inlet and small pores (300 μm) at the outlet, whereas the uniform wick flow condenser has a medium pore size (570 μm) along its entire length. Despite the large pore sizes of the gradient wick structure at the inlet, the presence of a thin condensate film reduces the performance difference between the gradient and uniform wick flow condensers at the inlet compared to the condenser outlet.

6. Conclusions

In summary, the present study introduced a new strategy to the design of internal flow condensers for extremely wetting fluids operating under the filmwise heat transfer mode. Considering variations in the two-phase flow characteristics, the local topology of the flow condenser was tuned, resulting in a gradient wick structure with tailored flow condensation of low surface tension fluids. To evaluate the effectiveness of the proposed concept, the gradient wick flow condenser and its reference uniform counterpart of a similar average porosity were 3D-printed with stainless steel. Under a fully condensed state (i.e., an exit vapor quality of 0), a fixed cooling temperature potential of 5 °C, and a fixed flow rate of 0.1 g/s, the gradient wick flow condenser demonstrated a 26 % higher condensation heat transfer coefficient than its uniform counterpart (i.e., 0.97 versus 0.77 kW/m^2-K). Additionally, at a fixed normalized power density of ~1.3×10^{-6}, the gradient wick flow condenser offered a 21 % higher normalized power density compared to its uniform counterpart (i.e., 3.5 versus 2.9 kg/m^2-s) at a full condensation state. Furthermore, a semi-analytical flow condensation model was developed, shedding interesting physics associated with the gradient wick flow condenser. The local heat transfer coefficient of the gradient wick flow condenser increased along the condenser length despite the condensate film thickening, enabled by its progressively narrowing pore sizes in both longitudinal and lateral directions. This

stands in clear contrast to conventional flow condenser designs, including the uniform wick flow condenser, which shows a steady drop in heat transfer coefficient along the condenser length as the condensate film thickens. The outcomes of the present study highlight the critical role of the interplay between local topology and two-phase flow characteristics in the development of future flow condensers for low-surface-tension fluids, including dielectrics and refrigerants.

CRediT authorship contribution statement

Durga Prasad Ghosh: Writing – original draft, Visualization, Methodology, Investigation, Formal analysis, Data curation. **Vivek Mano Mohan:** Investigation, Data curation. **Mohammad Reza Shaeri:** Supervision, Project administration, Investigation, Funding acquisition, Conceptualization. **Sajjad Bigham:** Writing – review & editing, Supervision, Project administration, Methodology, Investigation, Funding acquisition, Conceptualization.

Declaration of competing interest

The authors declare that they have no known competing financial interests or personal relationships that could have appeared to influence the work reported in this paper.

Acknowledgements

This study was supported by the United States Office of Naval Research (ONR) under contract N68335-23-C-0464. The authors would like to thank Dr. Mark Spector for his support.

References

[1] P. Sarkiris, V. Constantoudis, K. Ellinas, C.W.E. Lam, A. Milionis, J. Anagnostopoulos, D. Poulikakos, E. Gogolides, Topography optimization for sustainable dropwise condensation: the critical role of correlation length, Adv. Funct. Mater. 34 (2024) 2306756, https://doi.org/10.1002/adfm.202306756.
[2] K. Fazle Rabbi, S. Khodakarami, J.Y. Ho, M.J. Hoque, N. Miljkovic, Dynamic omniphobic surfaces enable the stable dropwise condensation of completely wetting refrigerants, Nat. Commun. 16 (2025) 1105, https://doi.org/10.1038/s41467-025-56338-3.
[3] K.-S. Yang, K.-H. Lin, C.-W. Tu, Y.-Z. He, C.-C. Wang, Experimental investigation of moist air condensation on hydrophilic, hydrophobic, superhydrophilic, and hybrid hydrophobic-hydrophilic surfaces, Int. J. Heat Mass Transf. 115 (2017) 1032–1041, https://doi.org/10.1016/j.ijheatmasstransfer.2017.08.112.
[4] J.B. Boreyko, C.-H. Chen, Self-propelled dropwise condensate on superhydrophobic surfaces, Phys. Rev. Lett. 103 (2009) 184501, https://doi.org/10.1103/PhysRevLett.103.184501.
[5] N. Miljkovic, R. Enright, Y. Nam, K. Lopez, N. Dou, J. Sack, E.N. Wang, Jumping-droplet-enhanced condensation on scalable superhydrophobic nanostructured surfaces, Nano Lett. 13 (2013) 179–187, https://doi.org/10.1021/nl303835d.
[6] G.V. Durgam, S. Bigham, Gradient wick structures for enhanced thin film condensation of extremely wetting fluids, Appl. Therm. Eng. (2025) 127691, https://doi.org/10.1016/j.applthermaleng.2025.127691.
[7] J. Saple, B. Ahmadi, M.R. Shaeri, S. Bigham, Experimental study of a 3D-printed wick condenser for enhanced condensation heat transfer, in: 2024 23rd IEEE Intersoc. Conf. Therm. Thermomechanical Phenom. Electron. Syst., 2024, pp. 1–6, https://doi.org/10.1109/ITherm55375.2024.10709465.
[8] D.P. Ghosh, B. Ahmadi, V.M. Mohan, M.R. Shaeri, S. Bigham, Thermohydraulic characterization of 3D-printed metallic wick flow condensers, in: 2025 24th IEEE Intersoc. Conf. Therm. Thermomechanical Phenom. Electron. Syst., 2025, pp. 1–6, https://doi.org/10.1109/ITherm55376.2025.11235706.
[9] M.R. Shaeri, S. Bigham, V. Mohan, M. Demydovych, Additively manufactured stacked refrigerant-toWater condenser, in: 2025 24th IEEE Intersoc. Conf. Therm. Thermomechanical Phenom. Electron. Syst., 2025, pp. 1–8, https://doi.org/10.1109/ITherm55376.2025.11235620.
[10] M.R. Shaeri, S. Bigham, B. Ahmadi, M. Demydovych, Enhancing flow condensation with 3D-printed refrigerant-to-water condenser, (2025). https://doi.org/10.1115/HT2025-151883.
[11] M.R. Shaeri, S. Bigham, V. Mano Mohan, M. Demydovych, 3D-printed condensers with gradient wick structures to enhance filmwise condensation, (2025). https://doi.org/10.1115/IPACK2025-163657.
[12] T.-S. Wong, S.H. Kang, S.K.Y. Tang, E.J. Smythe, B.D. Hatton, A. Grinthal, J. Aizenberg, Bioinspired self-repairing slippery surfaces with pressure-stable omniphobicity, Nature 477 (2011) 443, https://doi.org/10.1038/nature10447.
[13] S. Anand, A.T. Paxson, R. Dhiman, J.D. Smith, K.K. Varanasi, Enhanced condensation on lubricant-impregnated nanotextured surfaces, ACS Nano 6 (2012) 10122–10129, https://doi.org/10.1021/nn303867y.
[14] S. Sett, X. Yan, G. Barac, L.W. Bolton, N. Miljkovic, Lubricant-infused surfaces for low-surface-tension fluids: promise versus reality, ACS Appl. Mater. Interfaces 9 (2017) 36400–36408, https://doi.org/10.1021/acsami.7b10756.
[15] J. Köhler Mendizábal, B.P. Singh, K.F. Rabbi, N.V. Upot, K. Nawaz, A. Jacobi, N. Miljkovic, Enhanced internal condensation of R1233zd(E) on micro- and nanostructured copper and aluminum surfaces, Int. J. Heat Mass Transf. 207 (2023) 124012, https://doi.org/10.1016/j.ijheatmasstransfer.2023.124012.
[16] K. Cheng, S. Kim, S. Lee, K.J. Kim, Internal dropwise condensation: modeling and experimental framework for horizontal tube condensers, Int. J. Heat Mass Transf. 83 (2015) 99–108, https://doi.org/10.1016/j.ijheatmasstransfer.2014.11.084.
[17] Y. Ding, L. Jia, Y. Zhang, Z. An, Investigation on R141b convective condensation in microchannel with low surface energy coating and hierarchical nanostructures surface, Appl. Therm. Eng. 155 (2019) 480–488, https://doi.org/10.1016/j.applthermaleng.2019.04.023.
[18] N.V. Upot, K. Fazle Rabbi, S. Khodakarami, J.Y. Ho, J. Kohler Mendizabal, N. Miljkovic, Advances in micro and nanoengineered surfaces for enhancing boiling and condensation heat transfer: a review, Nanoscale Adv. 5 (2023) 1232–1270, https://doi.org/10.1039/D2NA00669C.
[19] M. Ahlers, A. Buck-Emden, H.-J. Bart, Is dropwise condensation feasible? A review on surface modifications for continuous dropwise condensation and a profitability analysis, J. Adv. Res. 16 (2019) 1–13, https://doi.org/10.1016/j.jare.2018.11.004.
[20] C. Zhang, C. Shen, Y. Chen, Experimental study on flow condensation of mixture in a hydrophobic microchannel, Int. J. Heat Mass Transf. 104 (2017) 1135–1144, https://doi.org/10.1016/j.ijheatmasstransfer.2016.09.029.
[21] D. Orejon, O. Shardt, N.S.K. Gunda, T. Ikuta, K. Takahashi, Y. Takata, S.K. Mitra, Simultaneous dropwise and filmwise condensation on hydrophilic microstructured surfaces, Int. J. Heat Mass Transf. 114 (2017) 187–197, https://doi.org/10.1016/j.ijheatmasstransfer.2017.06.023.
[22] M.M. Derby, A. Chatterjee, Y. Peles, M.K. Jensen, Flow condensation heat transfer enhancement in a mini-channel with hydrophobic and hydrophilic patterns, Int. J. Heat Mass Transf. 68 (2014) 151–160, https://doi.org/10.1016/j.ijheatmasstransfer.2013.09.024.
[23] D.S. Antao, K.L. Wilke, J.H. Sack, Z. Xu, D.J. Preston, E.N. Wang, Jumping droplet condensation in internal convective vapor flow, Int. J. Heat Mass Transf. 163 (2020) 120398, https://doi.org/10.1016/j.ijheatmasstransfer.2020.120398.
[24] M.K. Bashar, K. Nakamura, K. Kariya, A. Miyara, Condensation heat transfer of R1234yf in a small diameter smooth and microfin tube and development of correlation, Int. J. Refrig. 120 (2020) 331–339, https://doi.org/10.1016/j.ijrefrig.2020.09.002.
[25] Y. Hu, S.A. Jajja, C.-M. Yang, S.F.Y. Motta, B.A. Fricke, K. Nawaz, In tube condensation of low global warming potential refrigerants in an axial micro-fin aluminum tube, Int. J. Refrig. 161 (2024) 221–241, https://doi.org/10.1016/j.ijrefrig.2024.03.001.
[26] S.M. Kim, I. Mudawar, Flow condensation in parallel micro-channels - part 2: heat transfer results and correlation technique, Int. J. Heat Mass Transf. 55 (2012) 984–994, https://doi.org/10.1016/j.ijheatmasstransfer.2011.10.012.
[27] N. Mattiuzzo, A. Berto, M. Azzolin, D. Del Col, Experimental analysis and modelling of R1233zd(E) condensation heat transfer and pressure drop in small diameter channels, Therm. Sci. Eng. Prog. 62 (2025) 103586, https://doi.org/10.1016/j.tsep.2025.103586.
[28] K.W. Lin, C.C. Wang, Enhanced condensation heat transfer for dielectric fluid within microchannel heat sink, Int. J. Heat Mass Transf. 106 (2017) 518–525, https://doi.org/10.1016/j.ijheatmasstransfer.2016.09.001.
[29] J.Y. Ho, X.W. Wang, K.C. Leong, Filmwise condensation of steam on vertical plates with novel pin fin arrays produced by selective laser melting, Int. J. Heat Mass Transf. 126 (2018) 652–666, https://doi.org/10.1016/j.ijheatmasstransfer.2018.05.063.
[30] J.Y. Ho, K.C. Leong, T.N. Wong, Filmwise condensation of steam on sinusoidal pin fin arrays: effects of fin height and fin pitch, Int. J. Heat Mass Transf. 130 (2019) 1004–1015, https://doi.org/10.1016/j.ijheatmasstransfer.2018.10.104.
[31] O.M. Zaki, R.A. Stavins, M. Wenzel, A. Musser, D. Sharar, S. Elbel, N. Miljkovic, W. P. King, Additively manufactured compact water-cooled refrigerant condenser, Int. J. Heat Mass Transf. 244 (2025) 126836, https://doi.org/10.1016/j.ijheatmasstransfer.2025.126836.
[32] B. Ahmadi, J. Saple, M.R. Shaeri, S. Bigham, 3D-printed converging wick flow condensers for low surface-tension fluids: modeling and experiment, Int. J. Heat Mass Transf. 255 (2026) 127754, https://doi.org/10.1016/j.ijheatmasstransfer.2025.127754.
[33] D. Patel, D.P. Ghosh, V. Mohan, M.R. Shaeri, S. Bigham, Performance evaluation of a 3D-printed multi-layer wick flow condenser, (2025). https://doi.org/10.1115/HT2025-155354.
[34] J. Zhang, B. Elmegaard, F. Haglind, Condensation heat transfer and pressure drop correlations in plate heat exchangers for heat pump and organic rankine cycle systems, Appl. Therm. Eng. 183 (2021) 116231, https://doi.org/10.1016/j.applthermaleng.2020.116231.
[35] G.A. Longo, A. Gasparella, R. Rartori, Experimental heat transfer coefficients during refrigerant vaporisation and condensation inside herringbone-type plate heat exchangers with enhanced surfaces, 47 (2004) 4125–4136. https://doi.org/10.1016/j.ijheatmasstransfer.2004.05.001.